Polymer 239 (2022) 124420

Contents lists available at ScienceDirect

Polymer

journal homepage: www.elsevier.com/locate/polymer

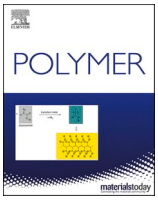

# Local structure mapping of gel-spun ultrahigh-molecular-weight polyethylene fibers

Mathias K. Huss-Hansen [a,1,2,*], Erik G. Hedlund [b,**,1], Anton Davydok [c], Marie Hansteen [a,d], Jildert Overdijk [d], Gert de Cremer [d], Maarten Roeffaers [b], Matti Knaapila [a,e], Luigi Balzano [d,***]

[a] Department of Physics, Technical University of Denmark, 2800, Kgs. Lyngby, Denmark
[b] cMACS, KU Leuven, 3001, Leuven, Belgium
[c] Institute of Materials Physics, Helmholtz-Zentrum Geesthacht, Notkestrasse 85, 22 607, Hamburg, Germany
[d] DSM, Applied Science Center, Urmonderbaan 22, 6167RD, Geleen, the Netherlands
[e] Department of Physics, Norwegian University of Science and Technology, 7491, Trondheim, Norway

ARTICLE INFO

*Keywords:*
Gel-spun polymer fibers
Skin-core structure
Fiber diffraction

ABSTRACT

We report on < 2 μm spatial resolution investigations of structural and morphological uniformity of aligned high-performance gel-spun ultrahigh-molecular-weight polyethylene (UHMWPE) fibers (thicknesses ranging from 60 μm to 300 μm) whose processing includes draw and quench. The degree of orientation of PE crystallites were found to increase near the surface of the fiber filaments (skin-core structure) in all samples when considering the $\langle P_2 \rangle$ orientation parameter calculated from wide-angle X-ray scattering (WAXS). The degree of orientation increases with drawn down ratio (keeping the quench temperature constant) and decreases with increasing quench temperature (keeping the draw down ratio constant). Orientation parameter values calculated from polarized Raman spectroscopy measurements of the symmetric C–C stretching (1130 $cm^{-1}$) bond of PE showed clear skin-core structure in the samples with the highest overall orientation. We also employ small-angle X-ray scattering computed tomography (SAXS-CT) to show that the morphology (on the length scale of tens of nm) exhibit clear skin-core structure in two of the samples. The thickness of the skin region (~12-17 μm) was estimated from the real-space SAXS morphology and found to be similar in undrawn and drawn filaments.

## 1. Introduction

Man-made fibers are found in products ranging from textiles, thermal insulation, and composite reinforcements to specialized applications in high-demand areas, including heavy-lifting, off-shore anchoring, ballistic protection, and bio-medical engineering.

Out of the fiber families, fibers made from ultra-high molecular weight polyethylene (UHMWPE) have the highest specific modulus and strength. The ultra-high strength of UHMWPE fibers was achieved with the invention of the gel-spinning process by Smith and Lemstra in the late 1970s [1–4]. In this process, UHMWPE ($M_w > 1 \times 10^6$ g/mol) is dissolved in a solvent, then spun and subsequently hot drawn at temperatures close to the melting point of the pure polymer.

The favorable mechanical properties of high strength fibers are directly related to the orientation and alignment of the molecules in the semi-crystalline structure [5]. In the ideal case, all the polymeric chains are oriented along the same direction, that is, along the fiber axis, and the axial strength of the fiber is limited by the polymer's molecular weight [6]. In order to achieve the highest mechanical properties, the process of spinning followed by drawing was established to preferentially orient the UHMWPE molecules along the fiber axis.

As discussed in the literature, the local molecular orientation and morphology can vary significantly within the fiber. For example, aramid fibers, including poly(p-phenylene terephthalamide) (PPTA) fibers, are known to exhibit skin-core morphologies [7–9], in which the core of the fiber possesses a higher degree of crystallinity than the fiber's outer

* Corresponding author.
** Corresponding author.
*** Corresponding author.
*E-mail addresses:* huss@mci.sdu.dk (M.K. Huss-Hansen), erik@physics.org (E.G. Hedlund), Luigi.Balzano@dsm.com (L. Balzano).
[1] M.K.H-H. and E.G.H. contributed equally to this work.
[2] Current address: Mads Clausen Institute, University of Southern Denmark, 6400, Sønderborg, Denmark

https://doi.org/10.1016/j.polymer.2021.124420
Received 28 July 2021; Received in revised form 23 November 2021; Accepted 29 November 2021
Available online 3 December 2021

layer, also known as the skin [8]. More importantly, a heterogeneous morphology along the radial direction of the PPTA fibers can be detrimental for their mechanical performance [7,8,10], since the breaking points of the fibers tend to be located near morphological boundaries (e.g., at the skin-core interface), as shown for PPTA in Ref. [8].

Skin-core morphology has also been observed and elegantly studied for gel-spun UHMWPE fibers by Ohta et al. [11]. The authors isolated individual filaments from the spinning line and showed detailed real-space images of the transverse filament cross-section by use of transmission electron microscopy (TEM). The TEM images revealed a heterogeneous morphology with a core region composed of typical shish-kebab superstructures [12,13] (consisting of two characteristic parts: a core of extended chain crystals, called the shish, along which several spherical chain-folded crystals, the kebabs, are located) in a solvent rich matrix and a polymer rich skin region composed so-called interlocked shish-kebab structures (i.e., the lamellae of neighboring shish-kebabs are intercalated) oriented along the fiber axis. Furthermore, the same authors have shown that these morphological heterogeneities are even more pronounced in filaments obtained at lower spinning speeds [14].

Spatially resolved X-ray scattering studies on polymer fibers are common, yet the literature is less comprehensive concerning fibers made from UHMWPE. In the typical scattering geometry, the fiber specimen is scanned by a narrowly focused X-ray beam (typical diameter on the order of a few μm) in the direction perpendicular to the fiber axis. Individual scattering patterns are then recorded at each position across the fiber. Riekel et al. [15] studied single PPTA fibers in this geometry to obtain maps of the degree of orientation of crystallites along the fiber axis. However, the scattering information obtained in this geometry is inherently smeared and contains information from the entire irradiated volume along the path of the X-ray beam. Roth et al. [16] used Monte Carlo simulations to model the projected scattering patterns, while Stribeck et al. [17,18] proposed using mathematical models to desmear the scattering information by exploiting the local fiber symmetry of the samples. Davies et al. [9,19] avoided the problem of radially smeared scattering patterns altogether by employing a different scattering geometry, in which fiber sections of 15 μm length were prepared by laser dissection and irradiated with the X-ray beam parallel to the fiber axis. Using this so-called “on-axis” geometry, information can be obtained on the crystallographic texture in the radial direction.

An emerging non-destructive method for studying spatially resolved structures is tomographic small-angle X-ray scattering (tomographic SAXS) [or SAXS computed tomography (SAXS-CT)] [20]. In this method, the sample is rotated while scattering projections are collected at different angles. These projection are then used to reconstruct the scattering from individual volume elements (voxels) inside the sample. State of the art SAXS-CT studies are commonly performed on materials that are resistant to radiation-induced damage, such as teeth [21] and bone [22,23]. Polymers are much more susceptible to radiation-induced damage, and thus the use of SAXS-CT is non-trivial on these systems due to the prolonged irradiation with the high energy X-ray beam. Schroer et al. [24] successfully used SAXS-CT to gain information about the local nanoscale structure inside an injection molded PE rod with a spatial resolution of 80 μm.

In this paper, we investigate the morphologies of gel spun UHMWPE fibers, prepared under specific processing conditions chosen to yield samples with distinct skin-core structures, by means of conventional and novel morphology sensitive analytical techniques. On one hand, we take advantage of the high spatial resolution (nm range) available with X-ray scattering in transmission mode, allowing for detailed morphological profiles along the transverse direction of the fibers. However, when operating in transmission mode, morphological information in the depth direction (parallel to the beam) is not directly accessible. On the other hand, to resolve morphology in the depth direction, we make use of Raman microscopy in confocal mode, which has recently gained attraction as a technique to resolve structural changes in fibers [25], to determine the local orientation distribution of the polymer chains inside UHMWPE filaments at a 3D resolution of less than 3 μm. Eventually, we validate the morphological picture that emerges by means of a novel X-ray tomography technique based on Small Angle X-ray Scattering Computed Tomography (SAXS-CT). We aim to increase the spatial resolution for the first time to less than 2 μm. This breakthrough will allow for a detailed investigation of thin specimens, for example UHMWPE filaments, and thereby push the applicability limit of SAXS tomography. We also discuss the resulting experimental challenges that needs to be addressed, including low scattering contrast and radiation damage. These complementary methods provide detailed understanding of the microscopic skin-core morphology in UHMWPE filaments.

## 2. Materials and methods

### 2.1. Solution-spinning of UHMWPE filaments

The filaments for this study were prepared by means of a monofilament spinning device (DSM R&D facilities, Geleen). In this process, an extruder is used to dissolve UHMWPE in decalin and pump the then formed gel through a spin hole to form a filament (see Fig. 1). The filament is then quenched in a water bath and wound on a bobbin after reaching room temperature. The bobbin is placed inside a fume-hood until the decalin is almost completely evaporated. In order to study the effect of processing conditions on features of the skin-core morphology, the temperature of the water bath and the filament draw down (DD) were systematically changed (see Table 1). The filament draw down is defined as the ratio between the speed of the first roller and the speed of the extruded filament (DD $= v_1/v_0$).

### 2.2. Polarized Raman spectroscopy

Polarized Raman spectra of the filaments were acquired using a MonoVista CRS+ (S&I Instruments) microscope following the sample positioning and experimental configuration found in the corresponding section of the supporting information. The approach targets a random position along the filament. At these positions, Raman spectra were acquired at varying depths along the radial direction of the filament, from the edge to the center. The spectra were acquired in two geometries with regards to the filament, and with a set laser power of 5–10 mW and an integration time of 5–10 s. The measurements were taken in two orientations: with the filament perpendicular to and parallel to the pump laser (i.e., side-on and on a cross-section of the filament, see Figs. S1-S2 in the supporting information). A 532 nm laser was used for pumping. For the side-on measurements, the microscope was imaging in air (40×, NA 0.75) directly into the filament, and for edge-on measurements, the filament was embedded in resin for stability and imaged directly in air. For the embedding process, the filament was attached to a

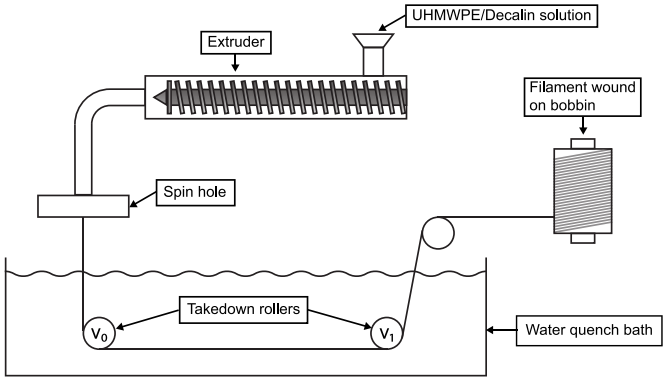


**Fig. 1.** Schematic illustration of the gel-spinning process of the UHMWPE filaments.

**Table 1**
Samples considered in the present study.

| Filament code | Draw dawn ratio | Water temperature (°C) | Nominal thickness (μm)[a] |
|---|---|---|---|
| DD1-low | 1 | 7.5 | 299 ± 7 |
| DD10-low | 10 | 7.5 | 65 ± 4 |
| DD1-high | 1 | 50 | 293 ± 26 |
| DD10-high | 10 | 50 | 94 ± 6 |

[a] Determined by measuring three random points along the fiber.

support and placed in a mold before pouring the resin under vacuum. After the mold had cured, it was polished until the smoothness and transparency of the surface was satisfactory for imaging. The sample spot was a diffraction limited volume, with width $< 0.4$ μm and depth $<$ 0.5 μm. Measurements were sampled $\geq 1$ μm apart (see supporting information) to ensure no overlap.

These measurements were then used to determine the orientation of the crystalline domains varies with respect to the filament depth. The analysis focuses on two key fingerprint regions of the PE spectrum listed in Table 2, namely the symmetric and asymmetric stretching of carbon-carbon bonds (1063 $cm^{-1}$ and 1130 $cm^{-1}$, respectively).

The analysis, described in the supporting information, gives us the true orientation parameters, $\langle P_2 \rangle$ and $\langle P_4 \rangle$, directly from the polarized Raman spectra. We use a modified version of the method laid out by Pigeon et al. [26], as described by Richard-Lacroix and Pellerin [27] and subsequently Kida et al. [28] and Hiejima et al. [29,30], to extract the orientation parameters. A related method, also described by Pigeon in the same article, uses the ratio between the intensity of the two aforementioned stretching modes. We use this to validate the calculated orientation parameters. Pigeon showed that this ratio is proportional to the orientation parameters, and a similar ratio-based method was recently used to accurately map the local crystallinity with high resolution in polyethylene terephthalate (PET) filaments [25].

### 2.3. Micro- and nanofocus X-ray scattering

Fig. 2a illustrates the experimental geometry employed for WAXS and SAXS experiments. WAXS measurements were performed at the MAX IV NanoMAX (Lund, Sweden) beamline [31]. A 13 keV X-ray beam was focused to 300 nm by 200 nm (horizontally × vertically) at the nominal sample plane. The diffraction patterns were recorded on a PILATUS 1 M detector (pixel size: 172 μm × 172 μm) positioned 471 mm downstream from the sample. The filaments were positioned as shown in Fig. 2a and WAXS patterns were collected by continuously scanning the filament through the beam along **r**. Images were collected every 500 ms, corresponding to the filament moving 1 μm. The detector had a down time between each measurement of 30 ms, during which there was no detection but the X-ray beam was still on and the stage still moved. However, since the path not covered by the detector during this time (= 60 μm) is smaller than the width of the beam, the entire filaments was still sampled. After completing one line scan, the sample was moved by 1 μm along the $z$-axis and a new line scan was performed with the same scan-range increment. In this way, a 2D map ($x$, $z$) of diffraction patterns was collected with a spatial resolution (or pixel size) of 1 μm × 1 μm. The individual diffraction patterns were too noisy to allow for detailed analysis of the crystalline orientation and were therefore averaged along the $z$-direction to give a statistical average. A detailed explanation of the methods used to calculate the orientation parameters of the PE crystallites from the WAXS data can be found in the supporting information.

**Table 2**
Raman fingerprint regions.

| Peak frequency ($cm^{-1}$) | Mode | Phase |
|---|---|---|
| **1063** | **Asymmetric stretching C–C** | **Crystalline** |
| **1130** | **Symmetric stretching C–C** | **Crystalline** |
| 1295 | Twisting CH2 | Crystalline |
| 1448 | Bending CH2, Fermi resonance | Amorphous |
| 1484 | Bending CH2, Fermi resonance | Amorphous |

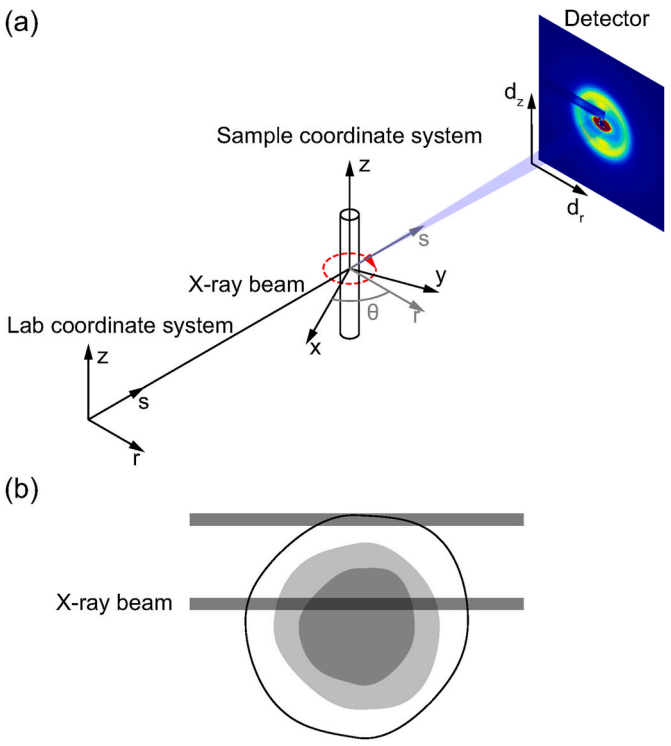


**Fig. 2.** (a) Experimental geometry of WAXS and SAXS-CT experiments. For WAXS, $\theta = 0$ and the sample coordinate axes are equivalent to the laboratory coordinate axes with $\mathbf{x} = \mathbf{r}$ and $\mathbf{y} = \mathbf{s}$. During the tomography experiment, the filament is rotated around **z,** and for each angle, the samples is scanned along **r** with scattering patterns collected at each point. The detector coordinates are $d_r$ and $d_z$. (b) Illustration of the X-rays path through the fiber in the employed geometry. The X-ray beam is probing a superposition of all the structures along its path and the recorded scattering projection is a projection of this superposition. The effect of the superposition is less significant close to the fiber surface.

SAXS-CT measurements were performed at the PETRA III Synchrotron (Hamburg, Germany) at the Micro- and Nanofocus X-ray Scattering beamline (P03) [32]. A 12.6 keV X-ray beam was focused to 1.4 μm × 1.4 μm at the sample position. The scattering images were recorded using a PILATUS 300 K detector (pixel size: 172 μm × 172 μm) placed 469 mm downstream from the sample. A custom-made beamstop allowed for a minimum **q**-value of 0.02 $Å^{-1}$ (maximum feature size of 32 nm). The filaments were positioned as shown in Fig. 2a and raster scanned though the X-ray beam along **r** in order to collect the tomographic projections with 1.4 μm step size and 500 ms exposure time per image. To ensure no deformation or movement of the sample during rotation, the filaments were mounted in a taut configuration to a custom 3D printed frame. Upon completion of a single projection, the filament was rotated by $\theta = 4°$ around its own axis and moved 1 μm along the $z$-axis, and the next projection was recorded. The stepping along the $z$-axis was included to minimize radiation induced damage in the sample during the scan due to prolonged exposure. 45 projections were collected in total, corresponding to a sample rotation of 180°. The sample transmission was measured separately by replacing the detector with a diode, and the resulting transmission data were used afterwards to normalize the scattering data and reconstruct the filament's attenuation coefficient. A detailed description of the tomographic problem and reconstruction is given in the supporting information along with discussion on potential radiation damage issues.

## 3. Results

### 3.1. Crystal orientation from WAXS

During the filament making process, the UHMWPE molecules undergo flow (in the extrusion die and during the eventual draw down) that is likely to transform into morphological orientation upon crystallization. To investigate the local orientation distribution of the crystalline phase, we made use of nanofocused WAXS. The geometry of the experiment is shown in Fig. 2a. The filaments are mapped perpendicular to the fiber axis and detailed analysis is performed by looking at the azimuthal profile of the 110 Bragg peak. Fig. 3 shows the calculated orientation parameter as a function of position from the filament surface for all samples. The Hermans' orientation parameter represents the degree of crystalline orientation about the filament fiber axis, with values ranging from −0.5 for complete perpendicular orientation to 1 for complete parallel orientation with a value of zero representing the isotropic case.

We would like to stress that the values shown in Fig. 3 are not representative of the actual radially-resolved orientation distribution of the crystalline phase (i.e., as a function of the filament radius), but rather represent the values calculated from a one-dimensional projection of a two-dimensional fiber slice. This distinction is inherent to the collection of the data. At every point, the beam passes through the entire longitudinal volume of the fiber slice and thus the resulting scattering pattern is a projection of this volume. The X-ray beam's path is illustrated on Fig. 2b. Since the filament cross-section is not cylindrically symmetric (this will become apparent later), it is not possible to apply mathematical models, such as the Abel transformation [17], to transform the projected data into true radial data. Nevertheless, the measured profiles give qualitative information about the local crystalline orientation distributions in the filaments.

From Fig. 3, it is immediately apparent that all four filaments show similar features in their $\langle P_2 \rangle_{WAXS}$ profiles, with less oriented crystals in the center region of the filament compared to the surface region (skin) of the filament.

DD10-low (high draw down ratio and low quench temperature) shows the highest overall crystalline orientation out of the four samples, with $\langle P_2 \rangle_{WAXS}$ values ranging from ~0.2 in the core to ~0.6 in the skin. On the other hand, the sample with low draw down ratio and high quench temperature (DD1-high) has the lowest $\langle P_2 \rangle_{WAXS}$ value in the filament core but the second highest value at the surface. DD10-high (high draw down ratio and high quench temperature) and DD1-low (low draw down ratio and low quench temperature) show similar values of $\langle P_2 \rangle_{WAXS}$ in core and skin, with the main difference being the relative thickness of the skin.

If we consider the skin of the filament to consist of points with $\langle P_2 \rangle_{WAXS}$ values above the mean $\langle P_2 \rangle_{WAXS}$ value of the core + 2 standard deviations, we can quantify the thickness of the skin in each of the four filaments. The thickness of the skin is comparable for filaments DD10-low and DD10-high at approximately 16 μm, while it is slightly larger for filament DD1-low (25 μm). The oscillatory decay of the DD1-high $\langle P_2 \rangle_{WAXS}$ profile leads to a skin thickness of either ~8 μm or ~21 μm, depending on whether or not the second peak at around 16 μm is considered part of the skin.

From these results, we can infer two trends of the crystalline orientation: the degree of crystalline orientation increases with drawn down ratio (keeping the quench temperature constant) and decreases with increased quench temperature (keeping the draw down ration constant).

One way to solve the issue of projected data is to do a full tomographic reconstruction of the filament. These results are presented in section 3.3.

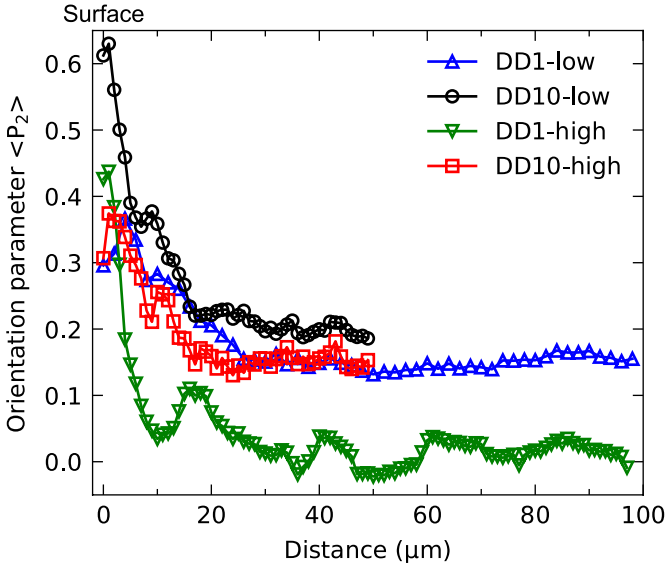


**Fig. 3.** Orientation parameter ($\langle P_2 \rangle$) profiles for all filaments calculated from the crystalline 110 reflection as measured by WAXS. Zero distance corresponds to the filament's surface.

### 3.2. Crystal orientation from a molecular perspective by microRaman

As a complementary method, microRaman was used to determine the depth-resolved orientation parameters of the molecular bonds. Fig. 4 shows profiles of the $h_{1130}/h_{1063}$ ratio together with the orientation parameters $\langle P_2 \rangle_{Raman}$ and $\langle P_4 \rangle_{Raman}$ as a function of sample depth for all four samples (from skin to core). For the samples with higher draw down, a clear non-uniform orientation profile is obtained: from core to skin, the extent of orientation increases steadily when getting closer to the edge. On the outside, there are indications that the orientation extent drops again (outer few μm). This is particularly visible in sample DD10-low, which had a low quench temperature. For the samples without draw down (DD1), an almost uniform orientation profile is obtained.

For all samples, the orientation profiles extracted from extensive $\langle P_2 \rangle$, $\langle P_4 \rangle$ determination qualitatively match those obtained from the method by Pigeon et al. ($h_{1130}/h_{1063}$ ratio), further confirming that this method can be used as a good and simple way to extract local orientation information in PE-based filaments.

Fig. 5 plots the $h_{1130}/h_{1063}$ ratio and $\langle P_2 \rangle_{Raman}$ profiles for all filaments to facilitate easy comparison with Fig. 3.

### 3.3. Reconstructed local morphology from SAXS-CT

Two of the four filaments were studied using SAXS-CT to obtain information about the local polymer morphology. We chose the DD1-high filament as the first sample because it showed the biggest difference in $\langle P_2 \rangle_{WAXS}$ from skin to core. We subsequently chose the DD10-high filament as the second sample to represent the high draw down case. Using the reconstruction technique described in the supporting information, we have reconstructed the entire 2D scattering pattern for every voxel inside the two filaments.

Fig. 6 shows the results of SAXS analysis for the DD1-high and DD10-high filaments, while Fig. 7 shows examples of reconstructed scattering patterns at different locations inside the fibers marked by the black squares in Fig. 6a and b. The reconstructions correspond to real-space slices of the fiber of approximately of 20 μm in thickness.

For DD1-high, the reconstructed scattering patterns (Fig. 7a) indicate a change in the local filament morphology when moving from the core towards the surface. The first (leftmost) scattering pattern, taken from the filament core, shows a mostly isotropic scattering ring at $q \approx 0.5$ Å$^{-1}$, indicating morphology of randomly oriented alternating crystalline lamellae and amorphous regions. The second pattern, taken from a position approximately 2/3 of the way towards the surface of the filament, shows a similar isotropy. Towards the filament surface, we begin to

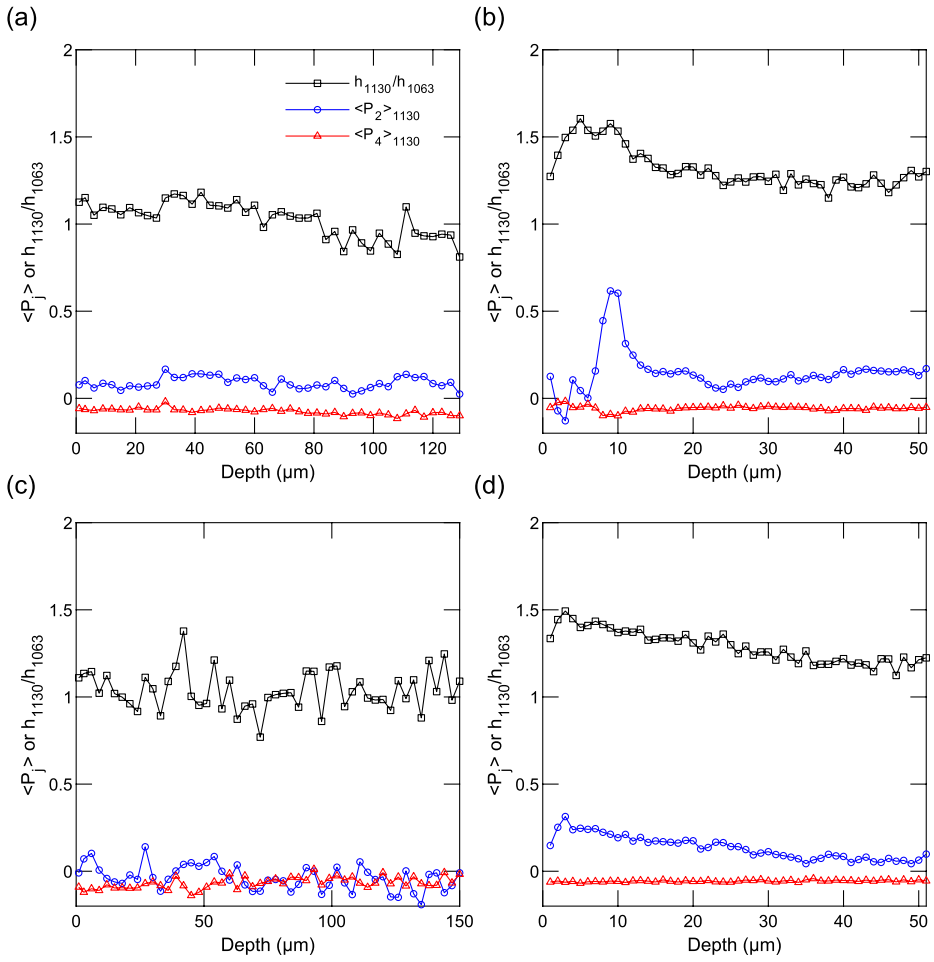


**Fig. 4.** Ratio of $h_{1130}/h_{1063}$ and orientation parameters profiles as calculated by polarized Raman spectroscopy for samples (a) DD1-low, (b) DD10-low, (c) DD1-high, and (d) DD10-high. Zero refers to the filament edge.

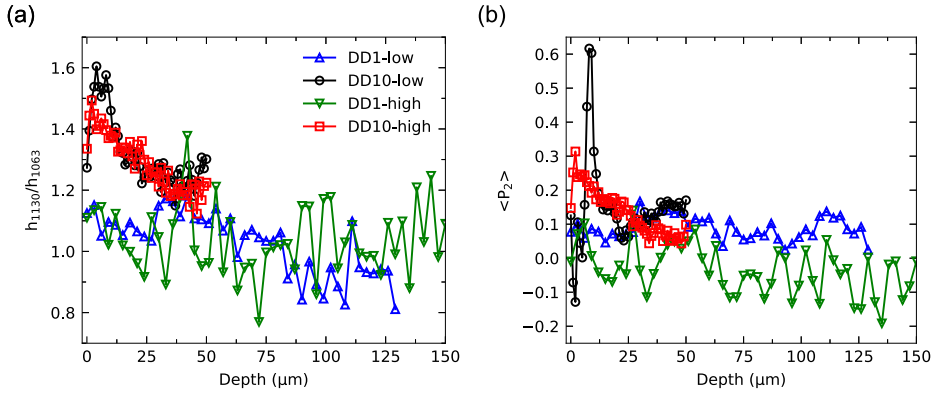


**Fig. 5.** Comparisons of (a) $h_{1130}/h_{1063}$ and (b) $\langle P_2 \rangle$ profiles for all filaments.

observe a change in the patterns from isotropic to anisotropic. At the third position, the scattering feature takes an oval shape with increased intensity along the meridional, indicating a gradual alignment of the lamellae with the stacking direction is perpendicular to the fiber axis. At the fourth position near the filament surface, we begin to observe two distinct lopes along the meridional, which become clearly separated at the outermost position (rightmost image in Fig. 7a). The emerging streak at the equatorial near the filament surface can be associated with the presence fibrillar scatterers oriented along the fiber axis. This suggests a morphological transition to predominantly shish-kebab superstructures near the fiber surface. Alternatively, although less likely, the scattering streak could also suggest the presence of elongated microvoids in the sample.

On the other hand, for DD10-high, the reconstructed scattering patterns everywhere inside the fiber posses some degree of anisotropy (Fig. 7b). We stress that, owing to the lack of rotational invariance in the sample (see supporting information), the correctness of the reconstruction along the equatorial is not guaranteed. In the skin of the filament (first and fifth pattern), two clear diffraction peaks are found along the meridional along with an intense scattering streak along the equatorial,

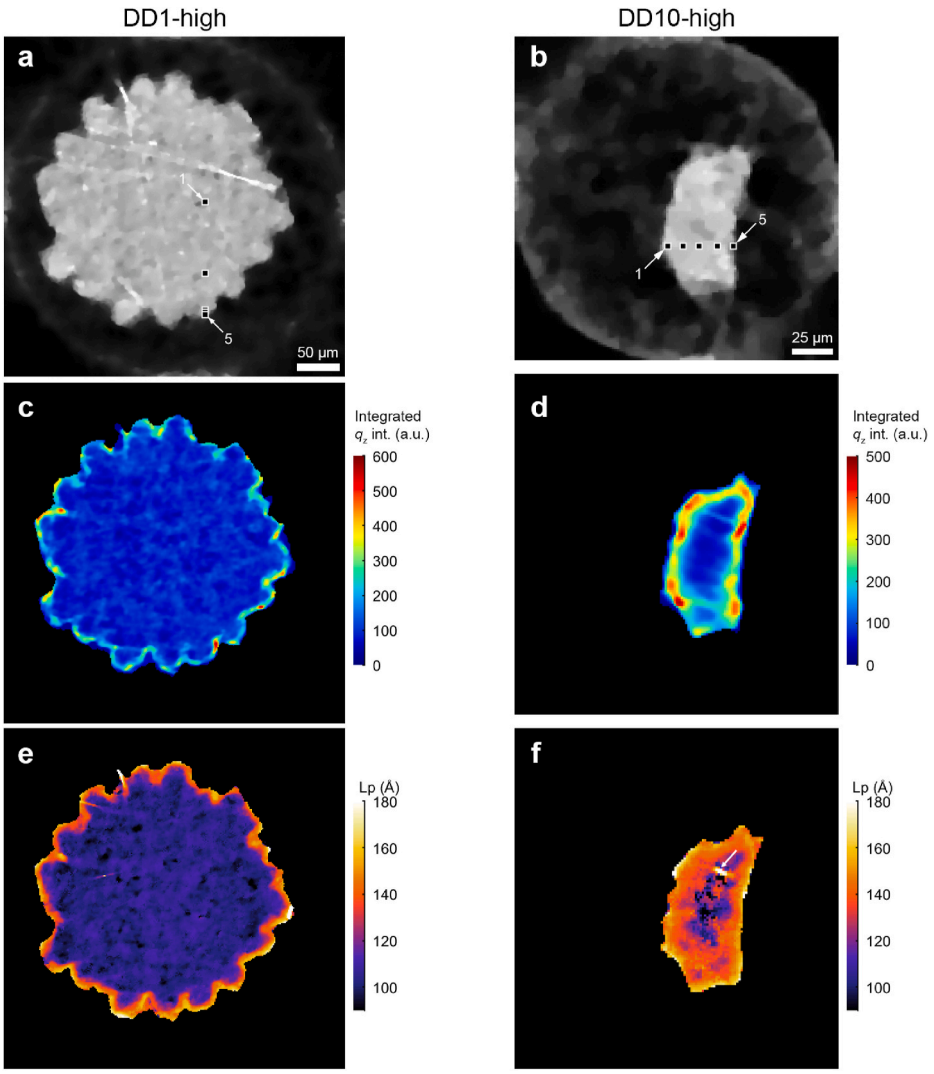


**Fig. 6.** Comparison of reconstructed SAXS morphology between filaments with high quench temperature. The panels on the left (a–c) are from the filament without drawndown (DD1-high) and the panels on the right are from the filament with drawdown (DD10-high). (a,d) Sample attenuation reconstructed from transmission measurement. Black squares represent voxels from which the scattering patterns in Fig. 6 are taken. (b,e) Integrated scattering intensity along the $q_z$ axis. (c,f) Lamella long-period from 1D correlation function analysis. The arrow in (f) marks a low **q** reconstruction artifact that gives rise to an erroneous 1D-correlation function. Each pixel corresponds to a size of 1.4 μm × 1.4 μm.

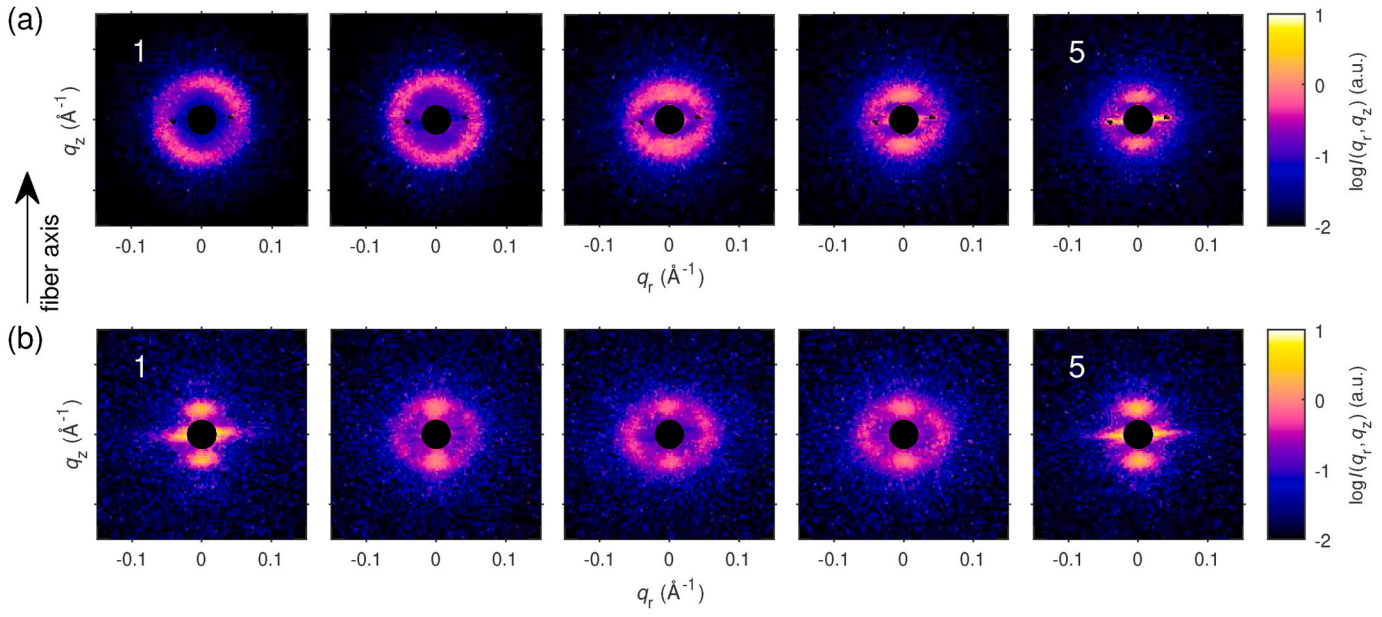


**Fig. 7.** (a) Example SAXS patterns of DD1-high filament reconstructed from positions indicated by squares in Fig. 5a. (b) Example SAXS patterns of DD10-high filament reconstructed from positions indicated by dots in Fig. 5d.

typically associated with shish-kebab superstructures. The extended chains of the shishes are highly oriented, forming densely packed fibrillar crystals and giving rise to the equatorial streak, while the chain-folded lamellae are stacked perpendicular to the fiber direction (giving rise to the meridional lopes). In the core region, the scattering appears less anisotropic with an insotropic scattering ring superimposed on top of the two meridional lopes. These features are also present in the raw projection data (not shown), indicating that the reconstructed patterns are quantitatively representative of their true counterpart.

For both samples, the reconstructed attenuation coefficient (Fig. 6a and b), represented here as gray-scale values between zero and one (normalized to the highest value), is found to be uniform throughout the entire cross-section. The faint rings seen at the edges of the reconstructed volumes are artifacts of the limited projection reconstructions and low counting rate.

Fig. 6c and d shows the integrated scattering intensity along the $q_z$-axis ($-10^\circ \leq \chi \leq 10^\circ$). For both DD1-high and DD10-high, there is an increase in the $q_z$ intensity towards the fiber surface, indicating either increased polymer crystallinity or increased crystalline orientation (along the fiber axis). If we consider that the scattering patterns in both cases undergo changes from less anisotropic (isotropic in the case of DD1-high) to more ansitropipic towards the surface of the filaments, we conclude that the observed increase in integrated $q_z$ intensity is at least partially caused by increased alignment of the crystalline lamellae along the fiber axis.

We used standard 1D correlation function analysis to extract information about the lamellae long period (*Lp*). Fig. 6e and f show the resulting *Lp* maps. As already observed in the $q_z$ intensity maps, the *Lp* maps display obvious skin-core features with increased *Lp* in the skin region. For DD1-high, the *Lp* map (Fig. 6e) reveals a mostly homogeneous core with average interlamellar distance of $104.6 \pm 3.6$ Å. There is a gradual increase in *Lp* towards the filament surface, where the *Lp* reaches values of >180 Å. The *Lp* map of DD10-high (Fig. 6f) shows approximately values of 100 Å in the filament core and values greater than 150 Å in the skin. The spot marked with an arrow is a low **q** reconstruction artifact that give rise to an erroneous 1D-correlation function.

## 4. Discussion

### 4.1. Structural observations

Under the employed spinning conditions, all filaments display highly heterogeneous skin-core properties in the degree of crystalline orientation obtained from WAXS. For all samples, the crystalline orientation is higher towards the surface of the filaments. In the solution-spinning process, the orientation of the polymer chains is induced by the flow of the gel through the spinneret holes. In a first order approximation, the flow profile is uneven across the diameter of the spinneret hole due to the no-slip condition at the wall boundary. The shear stresses on the gel are maximized at the spinneret wall, and in turn, the chains extension during the flow is greater near the surface of the filament. Upon leaving the spinneret, the shear stresses are relaxed, and the polymer chains are subjected to relaxation. If the subsequent crystallization occurs on a timescale faster than the critical relaxation time, the flow-induced chain orientation is preserved in the final structure. Higher draw down speeds lead to additional extension of the fibers upon leaving the spinneret, causing a further extension of the chains and counteracting the chain relaxation. At the same time, lower quenching temperatures facilitate a faster crystallization of the polymer, leading to less loss of their flow-induced orientation. These considerations are reflected in the $\langle P_2 \rangle_{WAXS}$ profiles. Moreover, lower draw down speeds during spinning lead to thicker filament diameters in the quench bath. Ohta et al. [14] speculate that a thicker filament diameter of dry-spun UHMWPE filaments will lead to increased structural heterogeneity between skin and core due to poor heat transfer from the filament surface. The $\langle P_2 \rangle_{WAXS}$ profiles indicate that for the filaments quenched at high temperature (DD1-high and DD10-high), the filament with draw down 1 is less homogeneous perpendicular to the fiber axis than the filament with draw down 10. However, for the samples quenched at low temperature (DD1-high and DD10-high), we observe the opposite behavior. Our findings suggest that the speculated poor heat transfer at the surface of the dry-spun filaments of Ohta et al. [14] is not the dominant mechanism for the skin-core structure found in our wet-spun filaments, possibly due to better heat transfer at the surface during quench.

We speculate that cross-sectional shape of the DD1-high filament could be a result of rapid evaporation of solvent in the air gap between the spinneret and the quenching bath, and subsequent reduction in volume. The flattened cross-section of the DD10-high is caused by deformation of the filament when it passes over the takedown rollers. Only the DD10 filaments are subject to this deformation, as they arrive at the rollers with higher temperatures (due to the increased takedown speed).

### 4.2. Skin-core structure across multiple length scales

In the present study, we have employed different methods to investigate the local structure of UHMWPE filaments. Each of these methods operate on different length scales within the material and provide information on different aspects of the semi-crystalline structure. Raman spectroscopy explores the vibration of the molecular bonds and thus represent the smallest length scale probed in this study. In principle, Raman spectroscopy can discriminate between amorphous and crystalline phases in the polymer structure, however, the results presented within this study are limited to vibrational modes located in the crystalline domains. In the X-ray scattering techniques, the contrast is provided by the differences in electron density across a periodic structure (on the level of the crystal lattice for WAXS and on the level of the semi-crystalline superstructure for SAXS).

While first indications of skin-core morphology could be readily derived from the polarized Raman results, obtaining a quantitative picture on the local orientation differences is not straightforward with Raman micro-spectroscopy for a few reasons. Firstly, the spatial resolution in Raman microscopy is limited by the laws of diffraction (about 1 μm in *xy* and a few micrometers in *z*). It is also not routine to measure at the same location on a filament in two orientations, as would be necessary, since the filament needs to be cut and embedded in resin for the edge-on measurements. Hence, there will be some averaging imposed by the technique itself. Moreover, the irregular shape and heterogeneous density of the filaments causes additional loss in spatial resolution, affecting the effective spatial resolution on the edge for observing local orientation effects in such small samples. Secondly, in the current analysis, only molecular vibrations in the crystalline domain are targeted, and thus signal strength is highly dependent on crystallinity. This could explain less orientation differences could be identified in the draw down 1 samples. Nevertheless, for samples with the highest overall orientation, Raman microscopy does provide a laboratory scale, albeit less sensitive, alternative to the synchrotron techniques.

Of the two samples (DD1-high and DD10-high) studied by SAXS tomography, both exhibit skin-core properties in the semi-crystalline superstructure. One advantage of the real-space mapping provided by the SAXS reconstruction is that we can estimate the thickness of the skin in a straightforward manner. For at detailed description of how we do this, please see Figs. S11-12 and the corresponding text in the supporting information. The results are listed in Table 3. For DD1-high, we obtain the same skin thickness from both the *Lp* map and the integrated $q_z$ intensity map. This suggests that the increased inter-lamellar distance towards the filament surface follows the increased lamellar alignment somewhat closely. Moreover, the uncertainty on the calculated thickness values are significant (almost 50% in the case of the $q_z$ intensity), indicating that the skin thickness is not homogeneous along the filament's surface. For DD10-high, the skin thickness obtained from the *Lp*

**Table 3**
Skin region thickness as determined by SAXS-CT reconstructions of $q_z$ intensity and long period.

| Sample | Skin region thickness (μm) | |
|---|---|---|
| | $q_z$ intensity | Long period |
| DD1-high | 13.3 (4.0) | 12.6 (5.8) |
| DD10-high | 16.5 (6.6) | 12.9 (4.5) |

map differs slightly more from the thickness obtained from the integrated $q_z$ intensity map, with the former being approximately 3–4 μm thicker. However, we note that the two values fall within each others uncertainty range. Interestingly, the absolute values of the skin thickness for both samples are surprisingly similar, indicating that the draw down speed is not the dominant effect in the skin formation.

It is tempting to compare the skin thickness obtained from SAXS-CT against the skin thickness obtained from the $\langle P_2 \rangle_{WAXS}$ profile. However, such a comparison has its physical and experimental limits. First of all, the hierarchical structural organization at the WAXS and SAXS levels might differ radially across the fiber. Secondly, the orientation parameter profile obtained from WAXS is not a function of the filament radius, but rather a function of the entire filament volume illuminated by the X-ray beam when scanning perpendicular to the fiber direction, as previously mentioned. The reconstructed maps of the DD1-high filament emphasize the lack of cylindrical symmetry, and the path of the X-rays through the filament is therefore very dependent on the local edge contour, which can results in highly irregular profiles. That said, the $\langle P_2 \rangle_{WAXS}$ profiles suggest that all the filaments have similar sized skin regions in the range of ~10 to ~20 μm.

## 5. Conclusions

In this study, the local structure of gel-spun UHMWPE filaments was investigated as a function of draw down ratio and water quenching temperature by means of WAXS, polarized Raman spectroscopy and SAXS computed tomography.

The local orientation of PE crystallites was investigated by nanofocused WAXS and profiles of the $\langle P_2 \rangle$ orientation parameter were calculated from the 110 Bragg peak. These results show skin-core structures in all filaments under the employed spinning conditions, with an increase in crystalline orientation towards the filaments' surfaces. This skin-core structure is thought to originate from the flow of the polymer gel through the capillaries in the spinneret, which causes increased shear and thus higher chain alignment at the filament surface. The overall crystalline orientation was highest in filaments obtained with high draw down ratio or in filaments with low water quenching temperature. However, the results are not conclusive on the relationship between processing parameters and the degree of heterogeneity between skin and core regions.

Polarized Raman microscopy in confocal mode was able to discern skin-core structures in the filaments with highest overall degree of orientation of the molecular bonds in the crystalline phase, as calculated from the symmetric C–C stretching (1130 $cm^{-1}$), obtained using a draw down ratio of 10 during the spinning process. A simplified analysis method based on peak ratios, as proposed earlier by Pigeon, gave qualitatively similar results as the extensive $\langle P_2 \rangle$, $\langle P_4 \rangle$ orientation parameter calculations. Clear skin-core features were visualized in the samples with the highest overall orientation.

The real-space morphologies of two filaments were investigated in detail using SAXS-CT with a microfocused beam and micrometer spatial resolution. Both samples (low and high draw down and high water quenching temperature) showed skin-core structured morphology. The core of the low draw down filament was composed of isotopically orientated lamellar structures with an inter-lamellar distance of 104.6 ± 3.6 Å, while the skin was composed of lamellar structures (shish-kebab superstructures) preferentially aligned along to fiber axis with a greater inter-lamellar distance ($Lp > 180$ Å). On the other hand, the high draw down sample was composed of stacked chain-folded lamellae in the core and shish-kebab superstructures in the skin, with increased alignment and inter-lamellae distance in the skin. In both samples prepared with high quenching temperature, the skin was found to be highly irregular along the filament surface, with both samples having similar values for the average skin thickness regardless of the difference in filament diameter. Moreover, the skin thicknesses determined from the SAXS-CT reconstructions were found to be similar to the skin thicknesses estimated from the crystalline orientation profiles as measured by WAXS.

To sum up, we have shown that all of the methods (nanofocused WAXS, polarized Raman microscopy in confocal mode and microfocused SAXS-CT) can be used to study skin-core structures in UHMWPE fibers with high spatial resolution (< 2 μm), with each method having their own unique advantages and drawbacks. Nanofocused WAXS provides high resolution $\langle P_2 \rangle$ profiles, but suffers from inherent smearing of the data along the direction of the beam. Polarized Raman microscopy in confocal mode offers laboratory-scale measurements, but is less effective in samples with low overall orientation. Microfocused SAXS-CT enable real-space mapping of morphological features with high resolution, but it is a highly specialized and time-consuming technique prone to radiation damage issues.

## Funding sources

This work was in part supported by the Danish Agency for Science, Technology, and Innovation through the instrument center DanScatt.

## CRediT authorship contribution statement

**Mathias K. Huss-Hansen:** Conceptualization, Software, Formal analysis, Investigation, Writing – original draft, Visualization. **Erik G. Hedlund:** Software, Formal analysis, Writing – original draft, Visualization. **Anton Davydok:** Investigation, Resources, Writing – review & editing. **Marie Hansteen:** Investigation. **Jildert Overdijk:** Investigation, Validation, Writing – review & editing. **Gert de Cremer:** Validation, Resources, Writing – review & editing. **Maarten Roeffaers:** Validation, Writing – review & editing, Supervision. **Matti Knaapila:** Conceptualization, Writing – review & editing, Supervision, Project administration. **Luigi Balzano:** Conceptualization, Validation, Resources, Writing – review & editing, Project administration.

## Declaration of competing interest

The authors declare that they have no known competing financial interests or personal relationships that could have appeared to influence the work reported in this paper.

## Acknowledgements

We would like to thank Collin Tan Yong Xiang, who performed the initial Raman microscopy at KU Leuven, Florian Wieland of Helmholtz-Zentrum Geesthacht and Sven Kreisig from the DSM Applied Science Center (Geleen, NL) for discussions, and Ulf Johansson, Alexander Björling and Sebastian Kalbfleisch of MAX IV for experimental assistance with the WAXS experiments. We acknowledge MAX IV Laboratory for time on Beamline NanoMAX under Proposal 20 160 015. Research conducted at MAX IV, a Swedish national user facility, is supported by the Swedish Research council under contract 2018-07 152, the Swedish Governmental Agency for Innovation Systems under contract 2018-04 969, and Formas under contract 2019-02 496. We acknowledge DESY (Hamburg, Germany), a member of the Helmholtz Association HGF, for the provision of experimental facilities. Parts of this research were carried out at PETRA III. Beamtime was allocated for proposal I-20180761.

## Appendix A. Supplementary data

Supplementary data to this article can be found online at https://doi.org/10.1016/j.polymer.2021.124420.

## References


[1] P. Smith, P. Lemstra, B. Kalb, A. Pennings, Ultrahigh-strength polyethylene filaments by solution spinning and hot drawing, Polym. Bull. 1 (1979) 733–736.
[2] P. Smith, P.J. Lemstra, Ultrahigh-strength polyethylene filaments by solution spinning/drawing. ii. influence of solvent on the drawability, Die Makromol. Chem. 180 (1979) 2983–2986.
[3] P. Smith, P.J. Lemstra, Ultra-high-strength polyethylene filaments by solution spinning/drawing, J. Mater. Sci. 15 (1980) 505–514.
[4] P. Smith, P.J. Lemstra, Ultra-high strength polyethylene filaments by solution spinning/drawing. 3. influence of drawing temperature, Polymer 21 (1980) 1341–1343.
[5] L. Balzano, B. Coussens, T. Engels, F. Oosterlinck, M. Vlasblom, H. van der Werff, D. Lellinger, Multiscale structure and microscopic deformation mechanisms of gel-spun ultrahigh-molecular-weight polyethylene fibers, Macromolecules 52 (2019) 5207–5216.
[6] D. Sawai, K. Nagai, M. Kubota, T. Ohama, T. Kanamoto, Maximum tensile properties of oriented polyethylene, achieved by uniaxial drawing of solution-grown crystal mats: effects of molecular weight and molecular weight distribution, J. Polym. Sci., Part B: Polym. Phys. 44 (2006) 153–161.
[7] R.J. Morgan, C.O. Pruneda, W.J. Steele, The relationship between the physical structure and the microscopic deformation and failure processes of poly(p-phenylene terephthalamide) fibers, J. Polym. Sci. Polym. Phys. Ed 21 (1983) 1757–1783.
[8] J. Graham, C. McCague, O. Warren, P. Norton, Spatially resolved nanomechanical properties of kevlar ® fibers, Polymer 41 (2000) 4761–4764.
[9] R.J. Davies, C. Koenig, M. Burghammer, C. Riekel, On-axis microbeam wide- and small-angle scattering experiments of a sectioned poly(p-phenylene terephthalamide) fiber, Appl. Phys. Lett. 92 (2008) 101903.
[10] K. Şahin, J.K. Clawson, J. Singletary, S. Horner, J. Zheng, A. Pelegri, I. Chasiotis, Limiting role of crystalline domain orientation on the modulus and strength of aramid fibers, Polymer 140 (2018) 96–106.
[11] Y. Ohta, H. Murase, T. Hashimoto, Structural development of ultra-high strength polyethylene fibers: transformation from kebabs to shishs through hot-drawing process of gel-spun fibers, J. Polym. Sci., Part B: Polym. Phys. 48 (2010) 1861–1872.
[12] A.J. Pennings, A.M. Kiel, Fractionation of polymers by crystallization from solution, III. on the morphology of fibrillar polyethylene crystals grown in solution, Kolloid-Z. Z. Polym. 205 (1965) 160–162.
[13] J. Smook, A.J. Pennings, Elastic flow instabilities and shish-kebab formation during gel-spinning of ultra-high molecular weight polyethylene, J. Mater. Sci. 19 (1984) 31–43.
[14] Y. Ohta, H. Murase, T. Hashimoto, Effects of spinning conditions on the mechanical properties of ultrahigh-molecular-weight polyethylene fibers, J. Polym. Sci., Part B: Polym. Phys. 43 (2005) 2639–2652.
[15] C. Riekel, T. Dieing, P. Engström, L. Vincze, C. Martin, A. Mahendrasingam, X-ray microdiffraction study of chain orientation in poly(p-phenylene terephthalamide), Macromolecules 32 (1999) 7859–7865.
[16] S. Roth, M. Burghammer, A. Janotta, C. Riekel, Rotational disorder in poly(p-phenylene terephthalamide) fibers by x-ray diffraction with a 100 nm beam, Macromolecules 36 (2003) 1585–1593.
[17] N. Stribeck, U. Nöchel, A.A. Camarillo, Scanning microbeam x-ray scattering of fibers analyzed by one-dimensional tomography, Macromol. Chem. Phys. 209 (2008) 1976–1982.
[18] N. Stribeck, U. Nöchel, S. Fakirov, J. Feldkamp, C. Schroer, A. Timmann, M. Kuhlmann, SAXS-fiber computer tomography. method enhancement and analysis of microfibrillar-reinforced composite precursors from PEBA and PET, Macromolecules 41 (2008) 7637–7647.
[19] R.J. Davies, M. Burghammer, C. Riekel, Probing the internal structure of high-performance fibers by on-axis scanning diffractometry, Macromolecules 40 (2007) 5038–5046.
[20] J.M. Feldkamp, M. Kuhlmann, S.V. Roth, A. Timmann, R. Gehrke, I. Shakhverdova, P. Paufler, S.K. Filatov, R.S. Bubnova, C.G. Schroer, Recent developments in tomographic small-angle x-ray scattering, Phys. Status Solidi 206 (2009) 1723–1726.
[21] F. Schaff, M. Bech, P. Zaslansky, C. Jud, M. Liebi, M. Guizar-Sicairos, F. Pfeiffer, Six-dimensional real and reciprocal space small-angle x-ray scattering tomography, Nature 527 (2015) 353–356.
[22] M. Liebi, M. Georgiadis, A. Menzel, P. Schneider, J. Kohlbrecher, O. Bunk, M. Guizar-Sicairos, Nanostructure surveys of macroscopic specimens by small-angle scattering tensor tomography, Nature 527 (2015) 349–352.
[23] M. Georgiadis, M. Guizar-Sicairos, A. Zwahlen, A.J. Trüssel, O. Bunk, R. Müller, P. Schneider, 3d scanning SAXS: a novel method for the assessment of bone ultrastructure orientation, Bone 71 (2015) 42–52.
[24] C.G. Schroer, M. Kuhlmann, S.V. Roth, R. Gehrke, N. Stribeck, A. Almendarez-Camarillo, B. Lengeler, Mapping the local nanostructure inside a specimen by tomographic small-angle x-ray scattering, Appl. Phys. Lett. 88 (2006) 164102.
[25] E. Perret, O. Braun, K. Sharma, S. Tritsch, R. Muff, R. Hufenus, High-resolution 2d Raman mapping of mono- and bicomponent filament cross-sections, Polymer 229 (2021) 124011.
[26] M. Pigeon, R.E. Prud'homme, M. Pezolet, Characterization of molecular orientation in polyethylene by Raman spectroscopy, Macromolecules 24 (1991) 5687–5694.
[27] M. Richard-Lacroix, C. Pellerin, Accurate new method for molecular orientation quantification using polarized Raman spectroscopy, Macromolecules 46 (2013) 5561–5569.
[28] T. Kida, T. Oku, Y. Hiejima, K. hei Nitta, Deformation mechanism of high-density polyethylene probed by in situ Raman spectroscopy, Polymer 58 (2015) 88–95.
[29] Y. Hiejima, T. Kida, K.-H. Nitta, In situ monitoring of orientation parameters and orientation distribution functions of polyethylenesduring tensile tests, Macromol. Symp. 377 (2018) 1700020.
[30] Y. Hiejima, T. Okuda, K. Kono, K. hei Nitta, Orientation behavior and deformation mechanism of polyethylene gels during cold drawing determined by in situ Raman spectroscopy, Polymer 176 (2019) 30–37.
[31] U. Johansson, U. Vogt, A. Mikkelsen, NanoMAX: a hard x-ray nanoprobe beamline at MAX IV, SAVE Proc. (2013) 88510L. SPIE 8851.
[32] C. Krywka, J. Keckes, S. Storm, A. Buffet, S.V. Roth, R. Döhrmann, M. Müller, Nanodiffraction at MINAXS (p03) beamline of PETRA III, J. Phys. Conf. Ser. 425 (2013), 072021.